J Vis (2010) 13:49–60
DOI 10.1007/s12650-009-0011-8

REGULAR PAPER

Josué Sznitman · Thomas Rösgen

Visualization of low Reynolds boundary-driven cavity flows in thin liquid shells

Received: 10 March 2009 / Revised: 4 June 2009 / Accepted: 9 August 2009 / Published online: 8 January 2010

Abstract Classic examples of low-Reynolds recirculating cavity flows are typically generated from lid-driven boundary motion at a solid–fluid interface, or alternatively may result from shear flow over cavity openings. Here, we are interested in an original family of boundary-driven cavity flows occurring, in contrast to classic setups, at fluid–fluid interfaces. Particle image velocimetry (PIV) is used to investigate the structure of internal convective flows observed in thin liquid shells. Under the specific configuration investigated, the soap bubble's liquid shell is in fact in motion and exhibits sporadic local "bursts". These bursts induce transient flow motion within the cavity of order $Re \sim O(1)$. The combination of PIV and proper orthogonal decomposition (POD) is used to extract dominant flow structures present within bubble cavities. Next, we show that thermally induced Marangoni flows in the liquid shell can lead to forced, (quasi) steady-state, internal recirculating flows. The present findings illustrate a novel example of low-Reynolds boundary-driven cavity flows.

Keywords Cavity flow · Low Reynolds number · Liquid shell · PIV · POD · Marangoni flow

1 Introduction

In classic fluid dynamics' examples of cavity flows, flow separation and internal recirculation may be generated by movements of external solid boundaries or fluid shear layers. Such flows are known to include eddies, secondary flows, complex three-dimensional (3D) patterns and chaotic particle motions (Shankar and Deshpande 2000). In the limit of low Reynolds numbers, cavity flows occur under conditions of creeping motion such that their structure is governed by the equations of Stokes flow (Pan and Acrivos 1967; Sznitman and Rösgen 2008). Slow internal recirculation is typically induced by (1) the translation of one or more of the containing walls (Leong and Ottino 1989; Shankar 1997), (2) driven by a shear flow over the cavity (Higdon 1985; Shen and Floryan 1985), (3) generated by the action of surface tension gradients (Rashidnia and Balasubramaniam 1991), or alternatively (4) may be induced from acoustic streaming (Sznitman and Rösgen 2008). Experimentally, these reverse and separating flows have drawn considerable interest: from the pioneering photographic visualizations of Taneda (1979) to more recent studies using liquid crystal techniques (Rhee et al. 1984) or particle image velocimetry (PIV) (Ozsoy et al. 2005). While

J. Sznitman · T. Rösgen
Institute of Fluid Dynamics, ETH Zurich, 8092 Zurich, Switzerland

Present Address:
J. Sznitman (✉)
Department of Mechanical and Aerospace Engineering, Princeton University,
Princeton, NJ 08544, USA
E-mail: sznitman@princeton.edu

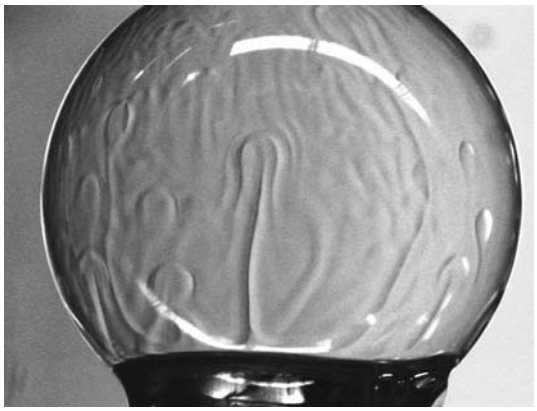

Fig. 1 Instantaneous visualization of buoyant vortices on the surface of the liquid film

in two-dimensional (2D) rectangular cavities, recirculating Stokes flows may exhibit corner vortices (Shankar 1993), the extension to 3D shapes involves a number of features that are absent from corresponding 2D motions (Tobak and Peake 1982), such as the occurrence of saddle points and the formation of open streamlines, present in recirculating flows in spherical cavities, that spiral into singular points (Pozrikidis 1994).

In analogy to the examples of low-Reynolds flows in cavities with solid boundaries, it is hypothesized that similar internal flow structures may possibly be present within thin liquid shells, such as simple air-filled soap bubbles. Indeed, film dynamics of such liquid shells are influenced, amongst others, by the interaction between (1) liquid thinning under the influence of gravity and (2) the presence of local surface tension gradients, which create flowing fluid layers in opposite direction to film draining (Couder et al. 1989; Sarma and Chattopadhyay 2001), as illustrated in Fig. 1. This later phenomenon is referred to as Marangoni flow (Scriven and Sternling 1960). At the interface between the liquid shell and the resident gas, the no-slip boundary condition holds such that internal flows would be induced during the motion of the shell. This would effectively yield an analogous configuration to that found in lid-driven cavity flows or to the Marangoni flow patterns in moving droplets and bubbles under the action of temperature gradients. Cavity flows illustrating a liquid–gas boundary, rather than a solid–gas one, are of particular relevance in biological processes. For example, pulmonary alveoli constitute the millions of sub-millimeter gas exchange units necessary for oxygen and carbon dioxide exchange between the lung and blood capillaries. These cavities are lined with a thin aqueous liquid layer (Bastacky et al. 1995) containing surfactant and are known to generate boundary-driven flows during breathing (Haber et al. 2000).

2 Experiments and data processing

2.1 Experimental setup

A sketch of the experimental setup is depicted in Fig. 2. Soap bubbles are generated at an orifice of radius $r_o = 1.5$ mm, by the expansion of a soap film into a thin liquid shell, through the use of a graduated syringe. The radius (R) of the soap bubble may be estimated based on the volume (V) pushed through the syringe using a spherical cap model (see Appendix). The syringe is filled with smoke particles, or alternatively with oil droplets, such that the cavity is effectively seeded. To minimize any disturbance in the flow initiated inside the soap bubble, the syringe plunger is cautiously displaced at a very slow pace. Furthermore, to avoid external flow disturbances, soap bubbles are placed inside a test cell with optical access, as described previously (Sznitman and Rösgen 2008). Internal bubble volumes are found in the range $V = 0.2$–0.7 ml, corresponding to bubbles with a radius $R = 3.5$–5.5 mm (see Appendix). The internal pressure within the bubble is slightly greater than the external atmospheric pressure. The pressure difference across the shell may be estimated as $\Delta P = 4\ \sigma/R$, where σ is the surface tension of the soap film (Roman et al. 2001). To increase the stability and life expectancy of the generated soap bubbles (bubbles can be maintained for up to several hours), a mixture composed of 1/3 distilled water, 1/3 commercial liquid detergent, and 1/3 glycerine is used (Eisenberg 1992). Typical soap bubbles have a film thickness in the order of 1 μm (Eisenberg 1992; Sarma and Chattopadhyay 2001). To avoid draining effects such as soap film accumulating in a pool at the

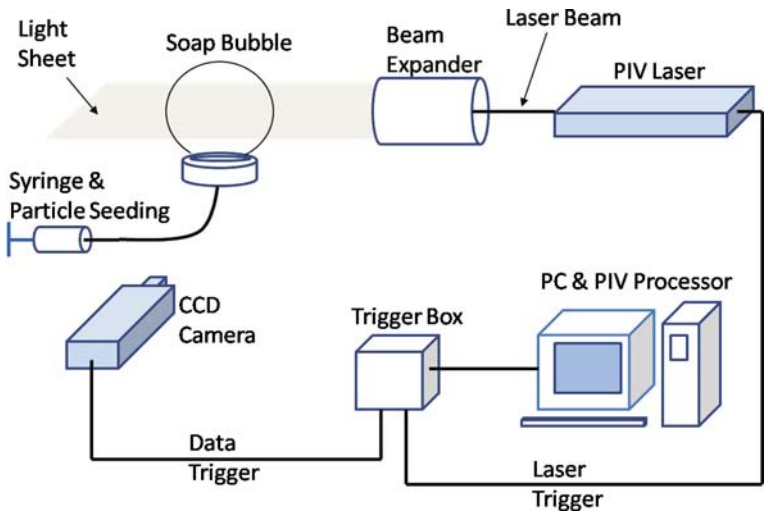

Fig. 2 Sketch of the experimental setup

bottom of the shell, bubbles are specifically oriented vertically upward above a retaining ring with attached drainage reservoir, rather than hanging downward.

The measuring equipment consists of a progressive scan CCD camera with 120 Hz image acquisition rate and a resolution of 640 × 480 pixels (Pulnix TM-6710), equipped with a Nikon macro lens ($f/\# = 2.8$, $f = 105$ mm). The laser sheet is generated by a 150 mW diode laser (830 nm, Lasisris Inc., Canada) making use of a beam expander. Due to the lighting and flow conditions, a pulsed illumination is not required; rather, consecutive images are recorded with an exposure time of 1/120 s each. To investigate whether a continuous laser illumination scheme induced motion in the liquid shell or in the cavity due to thermal effects, a pulsed illumination approach was also performed using a laser timer (LabSmith LC880 Programmable Experimental Controller). Over the measurement times considered, no significant changes in the bubble motion are observed. In particular, under thermal forcing, the characteristic flow patterns observed first with a continuous laser illumination are preserved (see Sect. 3.3, Fig. 11).

The soap bubble is geometrically described by a spherical cap and is therefore axisymmetric along the out-of-plane z-axis only. PIV measurements are conducted for two different planes cutting through the center of the bubble, as illustrated in Fig. 3a: (1) a horizontal x–y plane (top view) and (2) a vertical x–z plane (side view). The coordinate system is specified, where the origin is placed at the center of the spherical cavity (see Fig. 3b). Here, measurements in the horizontal and vertical plane are performed asynchronously. The inset of Fig. 3a shows a raw image with seeded particles undergoing rotational motion. Note that tracer particles appear sharper in the center region of the bubble, and increasingly blurry toward the bubble surface, where motion is largest. Such effects are due to relatively long camera exposure time and most visible in regions where flow velocity is highest. Finally, we experienced some laser light refraction due to the soap bubble surface. This led to small regions of flow measurement obstruction, in particular near bubble edges (e.g., Fig. 8). Further obstruction in the vertical measurement plane originated from refraction against the bubble orifice.

Planar vector displacement maps in each measurement plane are obtained with a standard PIV algorithm based on cross-correlation pattern matching with subpixel interpolation (Rösgen 2003). An interrogation window size of 32 × 32 pixel is chosen with a maximum window search size in x- and y-direction of 5 × 5 pixels and a window shift of 16 × 16 pixels, respectively. Given a CCD size of 640 × 480 pixels, and an image size of about 10.8 × 8.4 mm (which varies slightly depending on the bubble sizes investigated), the spatial resolution is approximately 0.017 mm and the total number of velocity vectors obtained is approximately 1,000, depending on the measurement plane considered. The exact scaling of the images is made possible by recording before each measurement, the image of a fixed reference scale. The temporal resolution is limited by the image acquisition rate (120 Hz) and series of image pairs were acquired for POD analysis over a length of up to several minutes.

2.2 POD analysis

The principal orthogonal decomposition (POD), also referred to as the Karhunen–Loeve expansion, was first introduced by Lumley (Lumley 1970) and is based on energy considerations. In particular, the snapshot

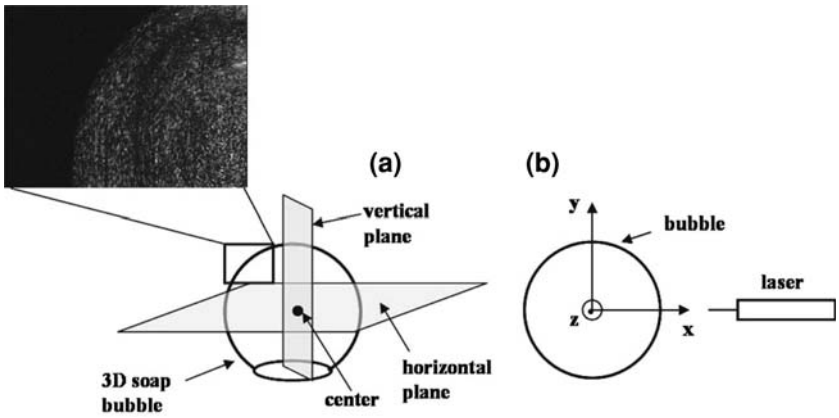

Fig. 3 **a** PIV measurement planes. *Inset* visualization of particle seeding inside the cavity. **b** Top view of the measurement field inside the membrane, including coordinate system. The origin is located at the center of the bubble

form suggested by Sirovich (Sirovich 1987) is useful in helping to recognize and characterize coherent structures and in analyzing comparatively small ensembles of large data vectors. For its application, spatio-temporal data are needed (i.e., a series of simultaneous 2D flow fields), which is provided by PIV. The following POD procedure follows closely that employed in previous PIV studies (Bernero and Fiedler 2000; Pedersen and Meyer 2002).

Any 2D field at time t_n is referred to as a snapshot, where the total number of snapshots is M. The data exist at discrete points on a rectangular grid in the horizontal plane, with N_x points in the x-direction and N_y points in the y-direction (or similarly N_z points in the z-direction when considering measurements in the vertical x–z plane). The average snapshot is calculated and subtracted from each member of the ensemble such that only the fluctuating part of all velocities in the domain for the nth snapshot remained. The average snapshot of the velocity field is calculated using:

$$\overline{\mathbf{u}}(\mathbf{x}) = \frac{1}{M}\sum_{n=1}^{M}\mathbf{u}(\mathbf{x}, t_n), \tag{1}$$

where $\mathbf{x}$ represents the discrete 2D spatial coordinates, (x, y), or respectively (x, z), in any snapshot. The resulting adjusted snapshots of the data representing the deviations from the mean are given by:

$$\mathbf{u}'(\mathbf{x}, t_n) = \mathbf{u}(\mathbf{x}, t_n) - \overline{\mathbf{u}}(\mathbf{x}). \quad n = 1, 2, \ldots, M. \tag{2}$$

Following the established procedure, a representation of the fluctuating PIV vector maps, $\mathbf{u}'(\mathbf{x}, t_n)$, is found based on an eigenvector/value decomposition of the covariance matrix,

$$\mathbf{u}'(\mathbf{x}, t_n) = \sum_{k=1}^{m}\lambda^{(k)}\theta^{(k)}(t_i)\sigma^{(k)}(\mathbf{x}). \tag{3}$$

In this notation, temporal (θ) and spatial (σ) eigenvectors are introduced, as well as the eigenvalues (λ). The eigenvalues permit the identification of energetically signification modes, and the following equation holds for the total kinetic energy present in the data,

$$E = \sum_{n=1}^{M}\|\mathbf{u}'(\mathbf{x}, t_n)\|^2 = \sum_{k=1}^{m}\lambda^{(k)^2}, \tag{4}$$

where the value of m specifies the number of basis modes included in the reconstruction. The POD decomposition is mathematically rigid, and the eigenmodes $\sigma(\mathbf{x})$ often show a strong "physical" behavior. Nevertheless, a direct interpretation of the eigenmodes in terms of relevant flow patterns is not always warranted. A more complete analysis would perhaps use some form of pattern recognition (e.g., adaptive clustering) to detect recurring combinations of the POD projection coefficients $\theta(t)$ and use these in a conditional averaging step. Applying this procedure to the present data did not, however, yield any significant change/improvement in the extracted flow patterns and the POD modes were kept as the basis of further interpretations.

3 Results and discussion

3.1 Instantaneous unforced flow fields

Instantaneous velocity vector maps reveal the existence of internal flows within the bubble cavity as shown in Fig. 4, in the vertical and horizontal planes, respectively. In particular, the liquid shell exhibits sporadic "bursts", which under the no-slip boundary condition at the liquid–gas interface induce locally the internal motion of the air residing in the proximity of the shell. Transient "bursts" observed along the shell generate tangential displacements, which, in turn, induce internal air flows circulating around the perimeter of the bubble. As a net result, the entire flow within the cavity must be displaced to fulfill the requirements of mass conservation, since the soap bubble approximates a closed spherical control volume (i.e., over the measurement times considered, the bubble volume remains unchanged, see also Sect. 3.3), giving rise to a slow recirculation motion bounded by the liquid shell. Local velocity gradients ($\mathrm{d}u/\mathrm{d}r$) in the radial direction ($r = 0$ at center of bubble) are clearly visible, where the velocity magnitude is largest at the shell surface ($r = R$) and $\mathrm{d}u/\mathrm{d}r > 0$ in the direction extending from the bubble center to the location of the burst. With PIV data, one may infer the origin and velocity of these "bursts" present on the shell by investigating the induced internal velocity field and recognizing that internal air flow motion results, indeed, from Marangoni-driven fluid layers in the thin film (i.e., bursts) due to surface tension gradients, as previously acknowledged (Couder et al. 1989; Sarma and Chattopadhyay 2001) (see also discussion at end of Sect. 3.1). Nevertheless, a direct correlation between motion in the gas and in the liquid is not available.

For the specific bubble configuration and dimensions investigated here ($R < 6$ mm), local velocities near the shell may yield during the transient of a burst, a magnitude of up to several mm/s (Fig. 4) depending on the measurement plane considered. At any time t_n, the mean spatial velocity magnitude in the measurement field considered may be given by

$$|\overline{\mathbf{u}(\mathbf{x}, t_n)}| = \frac{1}{N_x N_y} \sum_{i=1}^{N_x} \sum_{i=1}^{N_y} \left(u_x^2(i) + u_y^2(j)\right)^{1/2}, \tag{5}$$

(or respectively using w for measurements in the x–z plane), as illustrated experimentally in Fig. 5a. The resulting time-averaged value of the mean velocity magnitude may then be expressed as

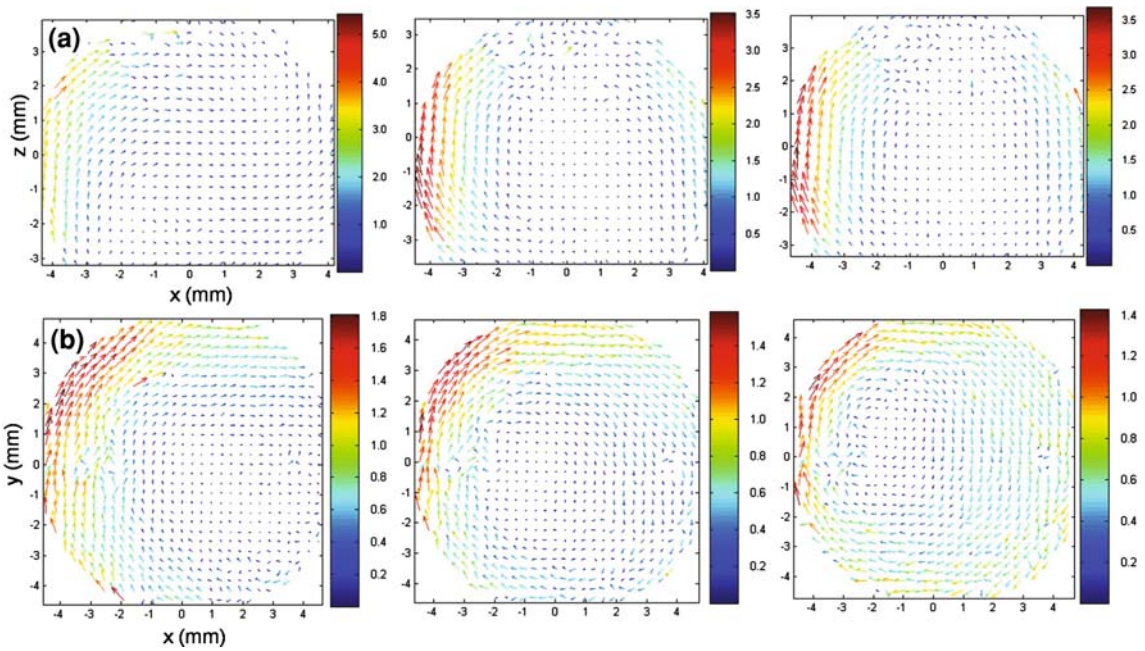

Fig. 4 From left to right: sequence of instantaneous vector maps in the **a** vertical and **b** horizontal plane. Scale is in mm/s. Note that measurements in **a** and **b** are asynchronous

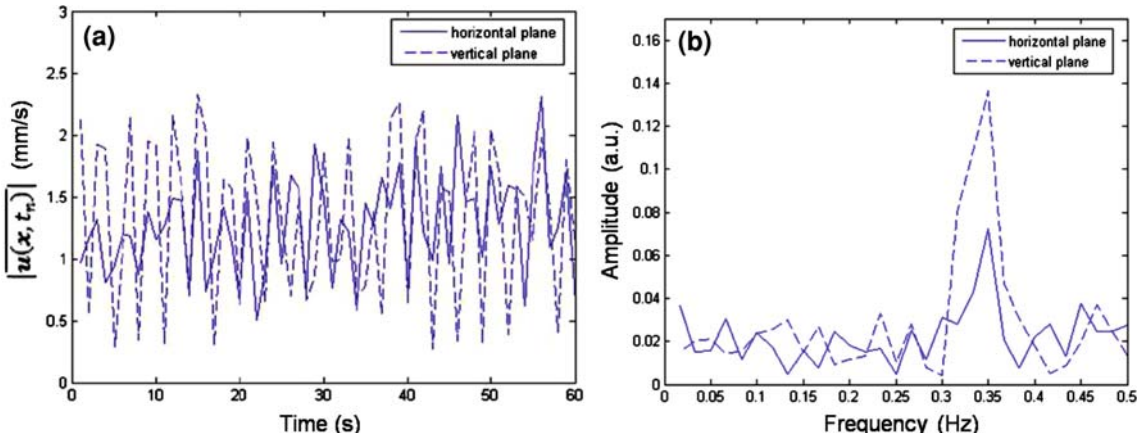

Fig. 5 **a** Temporal evolution of the mean spatial velocity in the horizontal and vertical planes for a 0.3 ml bubble (measurements are asynchronous). **b** Corresponding spectral amplitude obtained with a fast Fourier transform (FFT) in the horizontal and vertical plane

$$|\overline{\mathbf{u}}| = \frac{1}{t_m - t_1} \sum_{n=1}^{M} |\overline{\mathbf{u}(\mathbf{x}, t_n)}|. \tag{6}$$

where arbitrarily $t_1 = 0$. As seen in Fig. 5a, the internal cavity of these thin liquid shells is effectively characterized by the existence of net non-zero convective flows, which persist over time. For the measurements illustrated here, the time-averaged mean planar velocity magnitude yields in the order of $|\overline{\mathbf{u}}| \approx O(1.5)$ mm/s both in the horizontal and vertical plane. Qualitatively, flow recirculation is a transient process exhibiting temporal fluctuations in flow magnitude, due to the sporadic, but repetitious, motion of the liquid shell. One may note that locally, magnitudes of planar flow fields are observed to be slightly larger in the vertical plane compared to those seen in the horizontal plane. This may be due to the predominance of the shell motion in the vertical direction under the specific configuration investigated here (see discussion at end of Sect. 3.1). Concurrently, the vertical motion inside the cavity appears to be typically restricted to a local region near the shell (Fig. 4a), where flow motion in the horizontal plane is perhaps weaker in magnitude, but simultaneously appears to extend more globally over a larger region inside the bubble (Fig. 4b).

A spectral analysis of the temporal evolution pattern is obtained using a fast Fourier transform (FFT) of the transient signal $|\overline{\mathbf{u}(\mathbf{x}, t_n)}|$ of Fig. 5a. Results are reported in Fig. 5b for a 0.3 ml soap bubble, where the presence of a small, but distinct peak may be observed in the spectral amplitude in the vicinity of 0.35 Hz, for independent PIV measurements in the vertical and horizontal planes. Such findings suggest that an oscillatory behavior may be present inside the cavity. In particular, it is suspected that if such frequency peaks are indeed a consequence of recirculation inside the bubble, one could potentially expect a $|\overline{\mathbf{u}}|/R$ scaling. However, detailed testing of this hypothesis is beyond the scope of the present study. Here, rather, we focus on comparing temporal evolution patterns inside the soap bubble cavity between unforced and thermal forcing configurations (see results in Sect. 3.3). Hence, acknowledging the effect of viewing composite motions under an unknown projection angle, the different motions in the horizontal and vertical planes without external forcing indicate the existence of global rotations and internal toroidal vortex flows as dominant flow patterns.

Defining here the Reynolds number as $Re = D|\overline{\mathbf{u}}|/\nu$ following Pan and Acrivos for a cavity flow (Pan and Acrivos 1967), where, $D = 2R$ and ν is the kinematic viscosity of air, one sees that for the time-averaged mean velocity field ($|\overline{\mathbf{u}}| \approx 1.5$ mm/s), values of the Reynolds number are generally in the order of $Re \approx O(1)$ (for an 0.3 ml bubble, $D \approx 8.5$ mm). This result suggests that cavity flows within soap bubbles are indeed slow and governed by Stokes flow, where inertial effects are negligible. Therefore, internal flows will be driven provided local motion of the liquid shell persists over time, as experimentally observed (see example in Fig. 5a). In particular, this is also illustrated in the ensemble averaged velocity maps, which yield both in the horizontal and vertical planes a non-zero velocity field (Fig. 6). Note that in Fig. 6, we illustrate a "short term" average of the flow, rather than the average of a very large number of individual independent velocity maps.

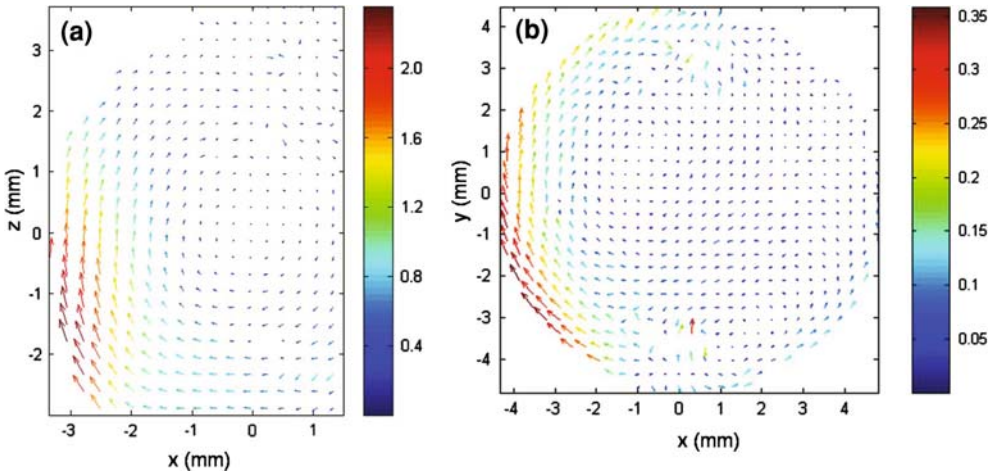

Fig. 6 Averaged vector maps of the flow field obtained from 100 instantaneous PIV vector maps in the **a** vertical and **b** horizontal plane. Scale is in mm/s

We open a short parenthesis to discuss briefly recirculating flow motion observed inside the soap bubble cavity in relation to the specific experimental configuration and orientation of the bubble. In the present study, soap bubbles are positioned vertically sitting on a base (i.e., ring) such that bubbles are truncated spheres (i.e., spherical caps), as discussed earlier in Sect. 2.1 (see schematic of setup Fig. 2). The vertical flowing fluid layers observed here and referred to as "bursts" have been detailed previously (Couder et al. 1989). In particular, buoyant motion seen presently resembles qualitatively that which may be observed in 2D vertical soap films, due to surface tension gradients resulting from spatially inhomogeneous distribution of surfactant in the film (compare Fig. 1 with vortices in Figs. 10 and 11 in Couder et al. 1989). While liquid film motion observed here (Figs. 4, 5, 6) may perhaps be a special feature resulting from the particular choice of the soap bubble orientation, Sarma and Chattopadhyay (2001) have reported, nevertheless, similar liquid film motion both in vertically as well as horizontally blown soap bubbles, where Marangoni convection-driven fluid flow due to surface tension gradients created by the stretching of the film to form a bubble was measured using spectrophotometry (Chattopadhyay 1999, 2000). In the present study, rather than monitoring the film motion and evolution through its thickness, we illustrate the feasibility of studying rather the resulting flows generated inside the soap bubble cavity, as a result of the no-slip boundary condition at the liquid–gas interface.

3.2 Dominant structures in unforced flow

We have made use of the POD technique to extract the dominant structures of the flow measured. The relative energy, $\lambda^{(k)^2}$, of POD modes 1–20 is compared to the total energy, E (Eq. 4), of the data set in Fig. 7 for asynchronous measurements in the horizontal and vertical planes of a 0.3 ml bubble. The first 20 modes capture, for both measurement planes, approximately 95% of the total energy. In particular, the first two modes capture over 85% of the total energy, while modes greater than number 3 remain under 1%. The curves decay rapidly at the beginning and become less steep for the higher mode numbers. The lower energy levels indicate smaller flow structures or noise, whereas the first, most energetic modes represent the dominant, large structures of the flow. In particular, the first mode alone captures slightly more than 60% of the total energy. Here, POD analysis is useful in emphasizing such flow structure, illustrated in Figs. 8i and 9i.

A selection of POD modes is shown, respectively, for the vertical and horizontal planes, in Figs. 8 and 9, where $\sqrt{\lambda^{(k)}}\sigma^{(k)}$ is plotted ($k = 1$–4). Hence, for each mode k plotted, the function $\sqrt{\lambda^{(k)}}\sigma^{(k)}$ has dimensions of a velocity magnitude and illustrates the relative importance of each mode, according to the magnitude of the eigenvalue $\lambda^{(k)}$.

The first two modes capture the relatively large-scale flow structures and, in particular, large vectors are visible near the region of the shell, which is in motion. Such dominant modes ($k = 1, 2$) correspond well with the averaged flow structures observed earlier in both measurement planes (Fig. 6). Moreover, recirculation regions are present within the core of the bubble. A relatively large vortex structure appears to be

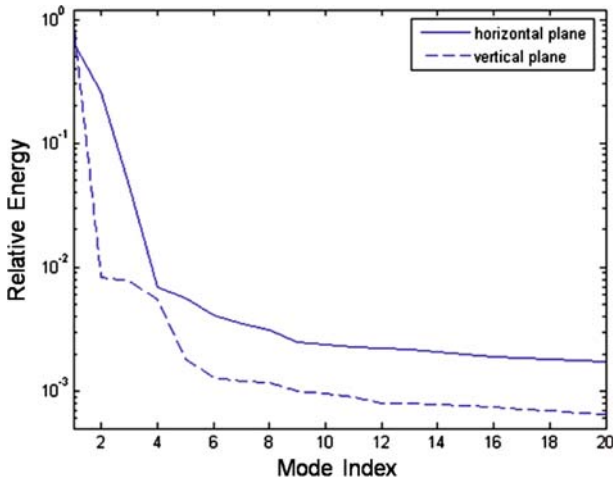

Fig. 7 Relative energy of first 20 POD modes for horizontal and vertical planes of a 0.3 ml bubble

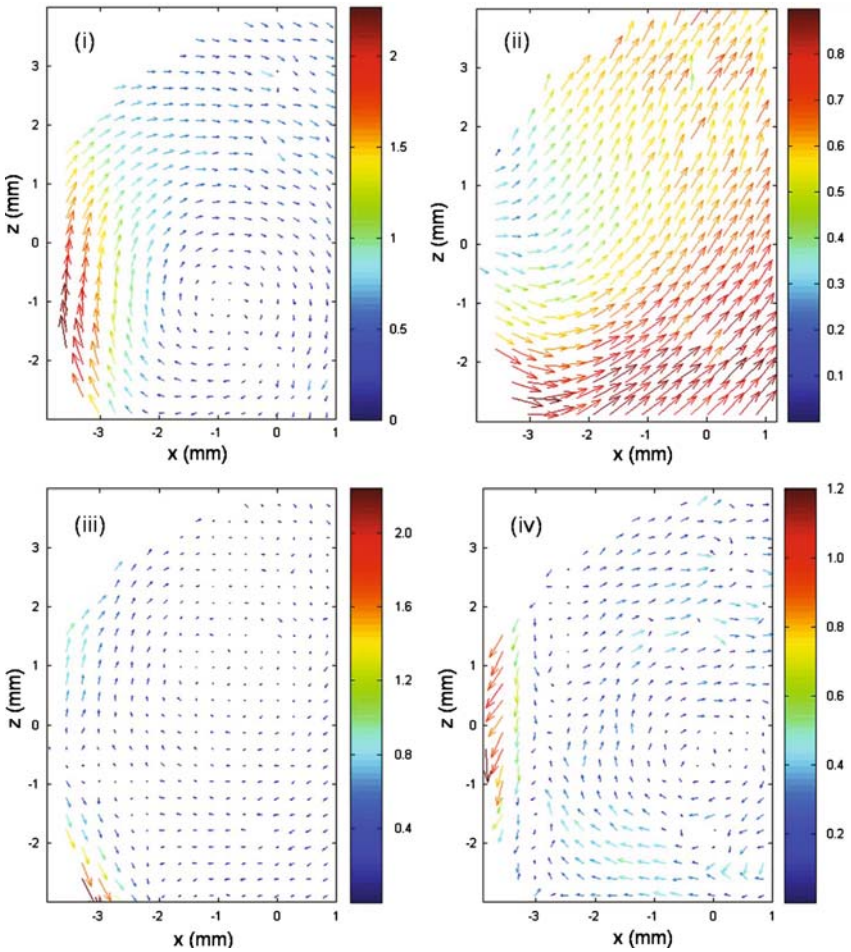

Fig. 8 POD modes (**i**)–(**iv**) for a 0.3 ml bubble (vertical plane). Small regions of flow obstruction are due to laser reflection on bubble surface. We have plotted $\sqrt{\lambda^{(k)}}\sigma^{(k)}$ with $k = 1$–4. Scale is in mm/s

present in the vertical plane (Fig. 8, mode 1) due to the local motion of the shell vertically upward, which induces a recirculation region in its proximity. A comparatively less energetic recirculation region is present in the horizontal plane, in the proximity of the moving shell, and therefore slightly off-centered relative to

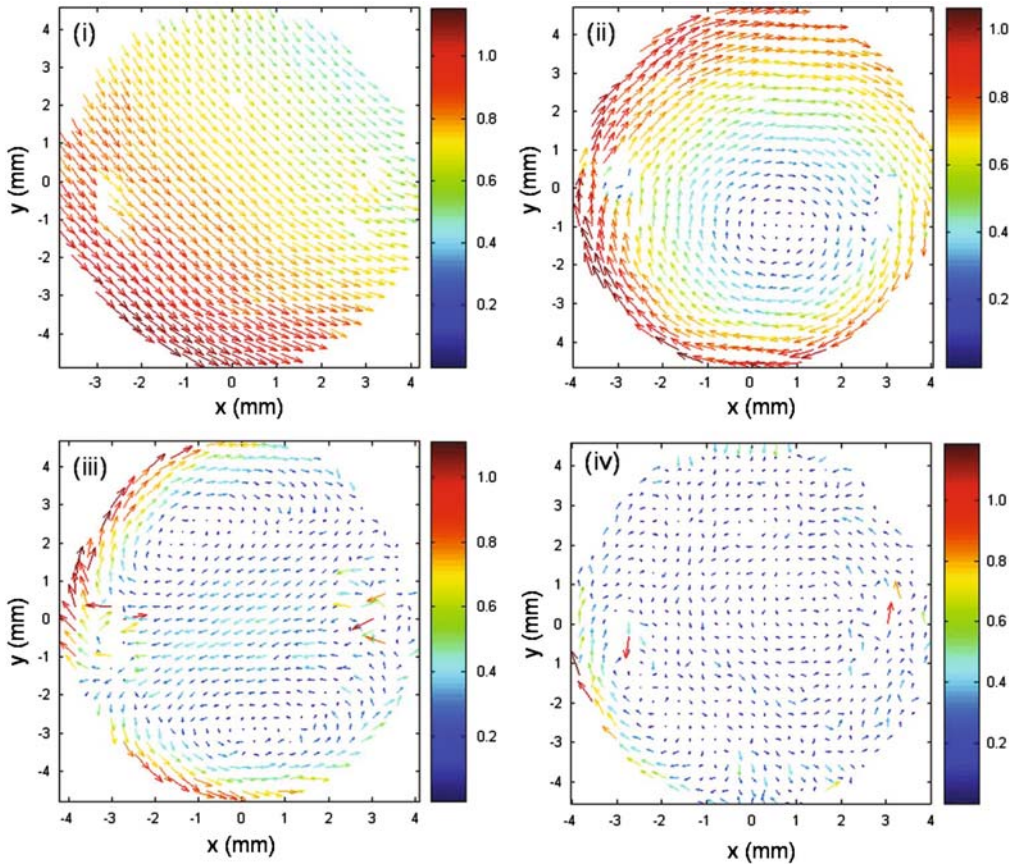

Fig. 9 POD modes (**i**)–(**iv**) for a 0.3 ml bubble (horizontal plane). Small regions of flow obstruction are due to laser reflection on bubble surface. We have plotted $\sqrt{\lambda^{(k)}}\sigma^{(k)}$ with $k = 1$–4. Scale is in mm/s

the origin of the bubble (Fig. 9, mode 2). In Fig. 9 (modes 2 and 3), it becomes clearer that the entire flow along the shell interface circulates in the horizontal plane.

The comparatively long delay (1 s) between the individual PIV maps should assure that there is only a limited amount of correlation in the ensemble, improving the statistical significance of the POD analysis, where a total of 60 independent vector maps are employed for the results illustrated in Figs. 7, 8, 9. The presence of a non-vanishing mean flow (Figs. 5a, 6) shows, however, that even longer observation intervals may be useful.

3.3 Thermally induced Marangoni flows

As observed experimentally here and reported previously for soap bubbles (Sarma and Chattopadhyay 2001), the Marangoni effect may induce local upward flow of liquid along the bubble film, depending on the orientation of the shell. This flow is driven by surface tension gradients that arise due to local gradients in surfactant concentration on the shell (Sarma and Chattopadhyay 2001), as discussed earlier (see Sect. 3.1). Under the no-slip condition at the liquid–gas interface, this phenomenon induces a boundary-driven flow inside the cavity. Similarly, it is well known that surface tension-driven (i.e., Marangoni) flows may be utilized for thin liquid film spreading in technological and biological processes (Cazabat et al. 1990; Kataoka and Troian 1999), by applying thermal gradients. Because most liquids maintain a negative and constant value of $\partial\sigma/\partial T$ where T is the temperature, the application of a constant thermal gradient produces a fixed viscous shear stress at the liquid surface given by $\tau = \nabla\sigma = (\partial\sigma/\partial)\nabla T$ (where ∇ is the vector differential operator), which in turn may provide the driving of a film, provided the upward flux due to thermal stresses is larger than the downward flux due to gravitational drainage, for the specific bubble orientation investigated here.

While soap bubbles may exhibit persisting, yet sporadic internal cavity flows, as has been shown for the present configuration, thermally induced Marangoni flows in a soap bubble film may potentially lead to

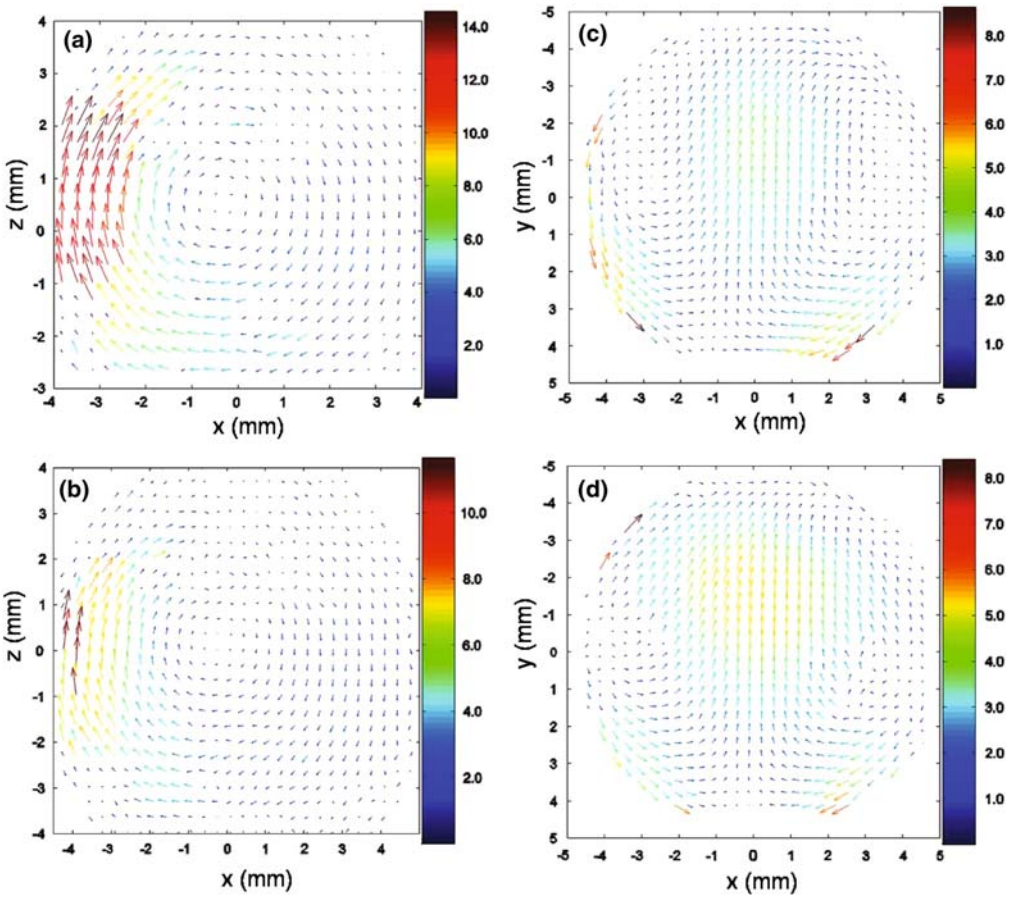

Fig. 10 Four examples of bubbles under thermal forcing. Heating source is located approximately at ($x = -4$ mm, $y = 0$ mm, $z = -1$ mm). Vector maps are obtained in the vertical plane, (**a**) and (**b**), and horizontal plane, (**c**) and (**d**), from ensemble-averaged PIV of 100 instantaneous vector maps. Scale is in mm/s

constant forced cavity recirculation. This may be achieved for example by providing locally a heat source in the vicinity of the liquid shell, such that a temperature gradient, ∇T, is effectively generated on the surface of the liquid shell. To support this hypothesis, we experimentally provide a heating source near the liquid shell at approximately ($x = -R$, $y = 0$, $z = R/4$) (coordinates are specified in Fig. 10), using a 3.3Ω resistor connected to a DC power supply. The resistor produces a local temperature gradient, with respect to the ambient surrounding, which is chosen between approximately 6 and 13°C (caution is taken not to apply too large temperatures near the thin film, which may lead to bubble rupture).

To guarantee that internal flow motion is generated by thermally induced surface tension gradients, rather than by buoyancy effects, a qualitative visualization of the liquid shell motion was first performed by seeding the thin film with titanium dioxide particles (TiO_2). This simple visualization scheme (not shown for brevity) is useful to illustrate two important features: (1) thermal forcing in the present configuration yields the driving of the liquid film (rather than directly inducing the motion of the internal flow); and (2) over the short measurement times considered, the thin liquid film represents nearly a shell of constant mass; no accumulation of the film is observed near the base.

Examples of ensemble-averaged velocity fields illustrating the internal flows under thermal forcing are shown in Fig. 10, respectively, in the vertical and horizontal plane. Thermally induced Marangoni flows in the liquid film lead to forced boundary-driven recirculation inside the cavity. In particular, an approximately constant temperature heat source leads to a relatively steady shear stress along the shell, such that flow fields are rather invariant over time. The cavity exhibits a strong recirculation region in the vertical plane, which rotates about the center of the bubble (Fig. 11 left), while the horizontal plane exhibits two closely symmetrical eddies (Fig. 11 right). Heating a spot on the side of the liquid shell reduces locally the surface tension of the soap film and drives it toward regions of higher surface tension. However, since the liquid film

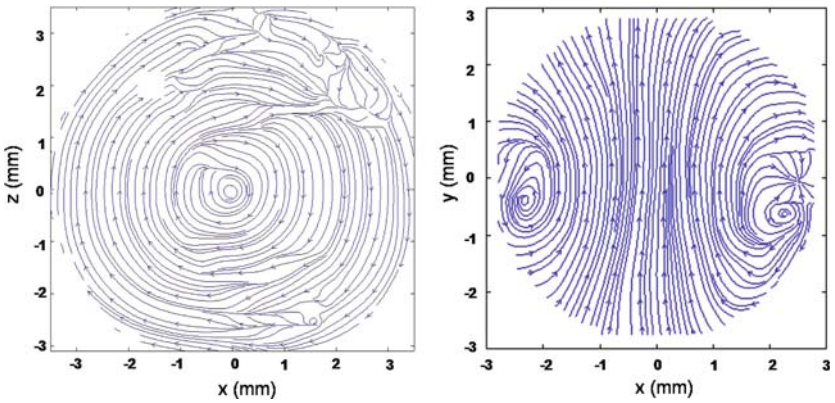

Fig. 11 Reconstructed internal streamline patterns under thermal forcing in the vertical (*left*) and horizontal plane (*right*). Results (*left*) are obtained using a pulsed laser illumination (see Sect. 2.1) and illustrate no significant differences in the flow patterns obtained in comparison with a continuous illumination approach

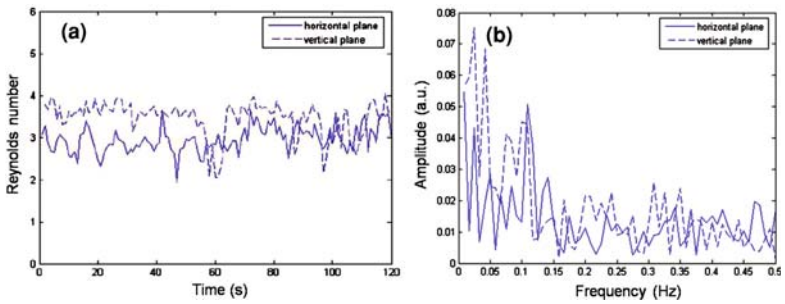

Fig. 12 Temporal evolution of the Reynolds number, *Re*, in the horizontal and vertical planes under thermal forcing (measurements are asynchronous) for a 0.4 ml bubble. **b** Corresponding spectral amplitude obtained with a fast Fourier transform (FFT) in the horizontal and vertical plane

represents approximately a shell of constant mass, the fluid flowing away from the heat source induces, following continuity, a reverse flow elsewhere on the surface. This, in turn, leads to the characteristic recirculation regions observed, which follows directly from the no-slip condition at the liquid–gas interface.

In Fig. 12a, the temporal evolution of the mean spatial velocity magnitude, $|\overline{\mathbf{u}(\mathbf{x}, t_n)}|$, is illustrated for the thermal forcing configuration in both measurement planes (plotted here as $Re = |\overline{\mathbf{u}(\mathbf{x}, t_n)}|D/\nu$, where $D \approx 9$ mm for an 0.4 ml bubble). The resulting mean flow magnitude appears to be slightly larger in the vertical plane, compared with that measured in the horizontal plane. In particular, for both measurement planes, the time-dependent Reynolds number is in the order of $Re \sim O(3)$ (see Fig. 12a), which is indeed larger than values obtained earlier under unforced conditions (see Fig. 5a). Moreover, the spectral analysis of the temporal mean velocity magnitude no longer reveals a distinct frequency peak in the signal (see Fig. 12b), indicating a different overall flow behavior compared to the sporadic "bursts" in unforced motion (Fig. 5b). Indeed, the spectral amplitude plots obtained for thermal forcing are relatively noisy with very low amplitudes. Hence, qualitatively speaking, it appears that a constant shear stress applied on the liquid shell generates rather clearly a (quasi) steady-state recirculating flow inside the cavity, where no apparent oscillatory behavior persists.

4 Conclusion

We have shown using PIV, in the present soap bubble configuration, that slow, recirculating cavity flows may exist inside a bubble without external forcing, due to sporadic, yet persisting, "bursts" in the liquid film, resulting from surface tension gradients. Additional information on the flow structures present inside the cavity is extracted using a POD analysis. Flow patterns appear to be governed by the motion of the liquid shell; recirculation regions are effectively induced in different planes of the bubble. Their location and strength are dependent on the velocity magnitude and exact location of the local displacements of the liquid

shell. The internal flows observed here at a liquid–gas interface exhibit similarities with classic setups of low-Reynolds number boundary-driven cavity flows at solid–fluid interfaces. Similarly, under thermal forcing, we find that Marangoni-induced flow motion in the liquid shell may yield (quasi) steady-state flow recirculation inside the soap bubble cavity. The flows observed here illustrate novel examples of internal low-Reynolds boundary-driven cavity flows.

Appendix

For a soap bubble of height, h, blown at an opening of radius, r_o, the volume, V, of the liquid shell is described by a spherical cap model such that (Harris and Stoker 1998):

$$V = \pi\left(\frac{1}{6}h^3 + \frac{1}{2}hr_o^2\right), \tag{7}$$

where $h = R + \sqrt{R^2 - r_o^2}$. For a given bubble radius, R, in the range of volumes considered (0.2–0.7 ml), the difference in volume relative to that of a sphere, where $V = 4/3\ \pi R^3$, remains below 10%.

References

Bastacky JL, Goerke CYC, Houshafar J, Yager H, Kenaga D, Speed L, Chen TP, Clements JA (1995) Alveolar lining is thin and continuous: low-temperature scanning electron microscopy of rat lung. J Appl Physiol 79:1615–1628

Bernero S, Fiedler HE (2000) Application of particle image velocimetry and proper orthogonal decomposition to the study of a jet in a counter flow. Exp Fluids 29:S274–S281

Cazabat AM, Heslot F, Troian SM, Carles P (1990) Fingering instability of thin spreading films driven by temperature gradients. Nature 346:824–826

Chattopadhyay A (1999) Molecules in a thin bubble membrane. Langmuir 15:7881–7885

Chattopadhyay A (2000) Time-dependent changes in a shampoo bubble. J Chem Educ 77:1339

Couder Y, Chomaz JM, Rabaud M (1989) On the hydrodynamics of soap films. Physica D 37:384–405

Eisenberg C (1992) The science of soap films. Dover Publication, NY

Haber S, Butler JP, Brenner H, Emanuel I, Tsuda A (2000) Shear flow over self-similar expanding pulmonary alveolus during rhythmical breathing. J Fluid Mech 405:243–268

Harris JW, Stoker H (1998) Handbook of mathematics and computational science. Springer, New York

Higdon JJL (1985) Stokes flow in arbitrary two-dimensional domains: shear flow over ridges and cavities. J Fluid Mech 158:195–226

Kataoka DE, Troian SM (1999) Liquid flow on the microscopic scale. Nature 402:794–797

Leong CW, Ottino JM (1989) Experiments on mixing due to chaotic advection in cavity. J Fluid Mech 402:463–469

Lumley JL (1970) Stochastic tools in turbulence. Academic Press, London

Ozsoy E, Rambaud P, Sitiou A, Riethmuller ML (2005) Vortex characteristics in laminary cavity flow at very low Mach number. Exp Fluids 38:133–145

Pan F, Acrivos A (1967) Steady flow in rectangular cavities. J Fluid Mech 28:643–655

Pedersen JM, Meyer KE (2002) POD analysis of flow structures in a scale model of a ventilated room. Exp Fluids 33:940–949

Pozrikidis C (1994) Shear flow over a plane wall with an axisymmetric cavity or a circular orifice of finite thickness. Phys Fluids 6:68–79

Rashidnia N, Balasubramaniam R (1991) Thermocapillary migration of liquid droplets in a temperature gradient in a density matched system. Exp Fluids 11:167–174

Rhee HS, Koseff JR, Street RL (1984) Flow visualization of a recirculating flow by rheoscopic liquid and liquid crystal techniques. Exp Fluids 2:57–64

Roman FL, Faro J, Velasco S (2001) A simple experiment for measuring the surface tension of soap solutions. Am J Phys 69:920–921

Rösgen T (2003) Optimal subpixel interpolation in particle image velocimetry. Exp Fluids 35:252–256

Sarma TK, Chattopadhyay A (2001) Simultaneous measurement of flowing fluid layer and film thickness of a soap bubble using a UV–visible spectrophotometer. Langmuir 17:6399–6403

Scriven LE, Sternling CV (1960) The Marangoni effects. Nature 187:186–188

Shankar PN (1993) The eddy structure in Stokes flow in a cavity. J Fluid Mech 250:371–383

Shankar PN (1997) Three-dimensional eddy structure in a cylindrical container. J Fluid Mech 342:97–118

Shankar PN, Deshpande MD (2000) Fluid mechanics in the driven cavity. Annu Rev Fluid Mech 32:93–136

Shen C, Floryan JM (1985) Low Reynolds number flow over cavities. Phys Fluids 28:3191–3202

Sirovich L (1987) Turbulence and the dynamics of coherent structures. Part 1: Coherent structures. Q Appl Math 45:561–590

Sznitman J, Rösgen T (2008) Acoustic streaming flows in a cavity: an illustration of small-scale inviscid flow. Physica D 237:2240–2246

Sznitman J, Rösgen T (2008) Acoustic streaming visualization in elastic spherical cavities. J Vis 11:347–355

Taneda S (1979) Visualization of separating Stokes flow. J Phys Soc Jpn 46:1935–1942

Tobak M, Peake DJ (1982) Topology of three-dimensional separated flows. Annu Rev Fluid Mech 14:61–85